

Frequency Conversion of Lasers in a Dynamic Plasma Grating

H. Peng^{1,2}, C. Riconda³, S. Weber^{4,5}, C.T. Zhou^{2,*} and S.C. Ruan^{1,2,†}

¹College of Physics and Optoelectronic Engineering, Shenzhen University, Shenzhen 518060, China

²Shenzhen Key Laboratory of Ultraintense Laser and Advanced Material Technology, Center for Advanced Material Diagnostic Technology, and College of Engineering Physics, Shenzhen Technology University, Shenzhen 518118, China

³LULI, Sorbonne Université, CNRS, École Polytechnique, CEA, F-75252 Paris, France

⁴Institute of Physics of the CAS, ELI-Beamlines Center, 18221 Prague, Czech Republic

⁵School of Science, Xi'an Jiaotong University, Xi'an, 710049, China

 (Received 1 March 2021; revised 29 April 2021; accepted 4 May 2021; published 24 May 2021)

When a dynamic medium in which the laser propagates changes its refractive index in time, the laser changes its frequency while keeping its wavevector unchanged to fulfill the dispersion relation. This is usually applied to upshift the laser frequency with ionizing plasma. We propose an alternative technique to modify light frequency. A transient plasma grating can be generated by two identical counterpropagating laser pulses via strongly coupled stimulated Brillouin scattering (SC SBS). The rapid evolution of the plasma grating affects the wave-dispersion relation and a band gap develops around the laser frequency, dependent on the grating amplitude. As a result, the lasers convert their frequency downward to the low edge of the band gap, while a free-traveling laser converts its frequency to both the upper and lower edge of the band gap. Depending on the considered setup, practical applications of this technique include either laser-frequency downshift or spectral splitting can be exploited. The former can be used for Raman amplification in plasma and the latter for dual-color x-ray generation by Thomson and/or Compton scattering.

DOI: [10.1103/PhysRevApplied.15.054053](https://doi.org/10.1103/PhysRevApplied.15.054053)

I. INTRODUCTION

It is well known that when the medium's refractive index changes in space, the electromagnetic wave (EMW) traveling inside the medium will change its wavevector while keeping its frequency to satisfy the changed dispersion relation. Similarly, if the refractive index is homogeneous in space, but has a temporal discontinuity, i.e., it changes rapidly in time, then the EMW's wavevector is conserved, but its frequency changes [1,2]. A rapidly created plasma around a monochromatic electromagnetic wave (by, e.g., flash ionization) causes part of the wave energy to be frequency upshifted to $\omega_1 = \sqrt{\omega_0^2 + \omega_{\text{PE}}^2}$, where $\omega_{0,1}$ are the original wave frequency and the upshifted frequency and ω_{PE} is the plasma frequency, respectively [3]. The electrons are suddenly set free and accelerated, they form a transverse current by following the electric field of the original EMW, which further induces a static magnetic field [4]. The frequency up-conversion is also called photon acceleration. It attracts a lot of attention because it is promising to

provide compact and coherent ultraviolet and x-ray laser sources with tunable frequency and bandwidth from the common visible and near-infrared laser [2,3,5–8]. The frequency-conversion phenomenon is also experimentally demonstrated in the microwave [9–11], terahertz [12], and visible-laser [13,14] regimes.

Recently, the general theory of frequency up-conversion has been reviewed and studied in detail [15,16]. A scheme of cascaded frequency up-conversion by flash ionization was proposed [17]. Particle-in-cell (PIC) simulations corroborate its potential to generate coherent ultraviolet and x-ray pulses at high efficiency and low cost. In experiments the extent of frequency up-conversion is limited, which is due to the fact that the ionizing pulse soon falls behind the photon-accelerated laser because of the discrepancy of the corresponding group velocities. However, the recently developed flying focus ionization [18] can overcome this disadvantage and convert an ultrashort optical pulse to the extreme ultraviolet within just a centimeter of propagation [19].

In this paper we propose an alternative method to modify light frequency in plasmas by exploiting the presence of a rapidly created and evolving plasma grating. A plasma grating is a spatially density-modulated periodic medium. Analogous to the solid photonic crystal, the refractive

*zchangtao@sztu.edu.cn

†scruan@sztu.edu.cn

index of the plasma grating alternates periodically in space, so it is also called a plasma photonic crystal [20,21]. It can be used as a plasma optical element to manipulate laser in both the nanosecond regime [22–24] or in the femtosecond regime [25]. The dispersion relation of EMW in a plasma grating is significantly different from that in vacuum or in a homogeneous plasma, i.e., it has a band-gap structure [20,26]. If a plasma grating is rapidly created in vacuum or from a homogeneous plasma, the EMW traveling inside the plasma grating will change its frequency and conserve its wavelength to obey the dispersion of the plasma grating. Experiments performed in the microwave range showed the possibility of converting the EMW to the eigenmodes of a rapidly created plasma grating (created by ionizing periodic gas jet) [27]. Plasma gratings can also be created rapidly by identical counterpropagating laser pulses in either underdense plasma [20,28,29] or on the surface of a solid target [30,31], with their spatial period being half of the pump-laser wavelength. Under the drive of the laser pulses, the dynamics of the plasma grating, its amplitude, and its lifetime can be determined to describe its growth, typical time of existence, and eventually collapse [29,32]. The same theory can be generalized to predict the behavior of gratings at the surface of an overdense plasma. During its lifetime, the grating can be used as a plasma optical device to manipulate short pulses. On longer time scales, however, the plasma grating is evolving, and its dispersion relation and band-gap structure also change accordingly. This implies continuous frequency conversion of the pump lasers or other EMWs traveling inside the dynamic plasma grating during its evolution.

In this work, we want to exploit this behavior to study the laser-frequency conversion in a rapidly created and fast-evolving plasma grating, driven by counterpropagating lasers via SC SBS in underdense plasma. In order to understand the frequency modifications in the presence of a grating, in Sec. II we consider a first ideal situation where the laser frequency is converted in a suddenly loaded time-invariant plasma grating whose space period is half of the laser wavelength (in accordance with the case in SC SBS). The laser frequency is found to be mainly converted to the edges of the lowest band gap and the frequency-converted lasers exist as standing Bloch modes in the plasma grating, closely following the theoretical predictions of eigenvectors and eigenmodes of light in such a system. The modes have zero group velocity and tend to localize in the plasma grating for a very long time. Then in Sec. III a more realistic situation is considered where a growing plasma grating is driven by lasers via SC SBS. In this case the band-gap width increases as the grating grows. In such a situation an injected test pulse will convert its frequency to closely follow the band-gap edges, in a similar way to the ideal case, as a result the pulse will be spectrally split. The frequencies of the lasers forming the grating instead are found to be mainly *downshifted* to the low edge,

while no significant up-conversion is found. This can be explained as being due to the spatial energy distribution of the beating counterpropagating pulses. Our results allow us to envisage various schemes of spectral splitting, upshifting, or downshifting laser pulses in plasmas depending on the chosen configuration.

Besides being intentionally generated to manipulate lights, fast-evolving plasma gratings driven by SC SBS are found in the laser speckles of fast-ignition inertial confinement fusion, which cause the formation of periodic reflectivity bursts, cavitons, and cavities, and the eventual saturation of SBS at a few percent of the pump-laser intensity [33–35]. Our findings in this work may facilitate better interpretations of the nonlinear behaviors of plasma gratings.

Notice that the generation of gratings by lasers in non-solid media has been investigated for some time [36–41] with experiments, simulations, and analytics. In this paper we consider laser-induced gratings in preformed plasma at much higher intensity. This can lead to strong modulations of the plasma and induces frequency conversion of the propagating intense laser.

The paper is organized as follows. In Sec. II, we first briefly review the matrix approach [42] to find the dispersion relation of a typical plasma grating. We then consider one-dimensional (1D) PIC simulations for an ideal situation where the plasma grating is then suddenly loaded around a free-traveling laser and two beating counterpropagating lasers. For both cases, the spectrum of the electric and magnetic field of the frequency-converted laser are analysed in detail. In Secs. III A, the frequency conversion of counterpropagating laser pulses, which drive a dynamic plasma grating via SC SBS is studied. Then in Secs. III B, we analyze the frequency conversion of a test laser. In Sec. IV, we discuss the possible applications of such a fast-evolving plasma grating. Finally, in Sec. V, the conclusions are drawn.

II. PRINCIPLE OF FREQUENCY CONVERSION IN A PLASMA GRATING

A one-dimensional nonlinear plasma grating can be treated as a multilayered medium with alternating stepwise density variation. As a model problem, we first consider a typical plasma grating, which is shown in Fig. 1(a). Its spatial period is Λ . In analogy with the case of a grating created by beating counterpropagating lasers, we consider that its period is related to the laser wavelength by the relation $\lambda_l = 2\Lambda$. The plasma density and width of the high-density (HD) and low-density (LD) layers are $n_1 = 1.2n_{cl}$, $d_1 = 0.2\Lambda$, $n_2 = 0.075n_{cl}$, $d_2 = 0.8\Lambda$, respectively. The average density is $n_0 = 0.3n_{cl}$, where $n_{cl} = m_e \pi c^2 / e^2 \lambda_l^2$ is the critical density corresponding to $\lambda = \lambda_l$.

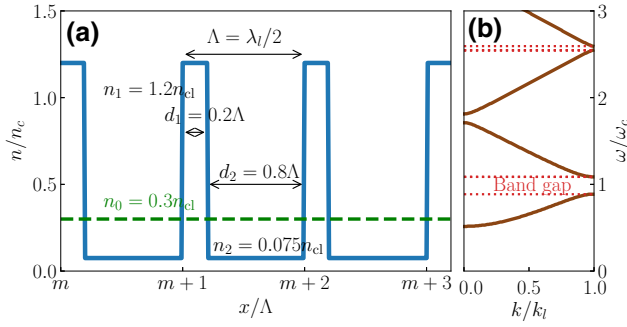


FIG. 1. A typical plasma grating from the m th layer to the $(m+2)$ th layer and its dispersion relation. (a) The blue line is the density outline of the plasma grating considered, the broken green line shows the average density. (b) The dispersion relation of the plasma grating. The red dotted lines outline the band gaps. Note that $k_l = 2\pi/\lambda_l$, $\omega_l = ck_l$, and $\omega_c = \omega_l\sqrt{1 + n_0/n_{cl}}$ is the central frequency of the band gap.

The dispersion of the plasma grating can be found by the so-called matrix approach [42]. Assuming the electrical field in the m th ($m \in \mathbb{N}$) unit grating can be written as $E_y(x, t) = E(x)e^{-i\omega t}$,

$$E(x) = \begin{cases} A_m e^{ik_1 \tilde{x}} + B_m e^{-ik_1 \tilde{x}}, & 0 < \tilde{x} < d_1; \\ C_m e^{ik_2 \tilde{x}} + D_m e^{-ik_2 \tilde{x}}, & d_1 < \tilde{x} < \Lambda, \end{cases} \quad (1)$$

where $\tilde{x} = x - m\Lambda$, $k_{1,2} = \sqrt{\omega^2 - \omega_{p1,p2}^2}$, ω_{p1} , and ω_{p2} are the plasma frequencies corresponding to n_1 and n_2 , respectively. Applying the boundary conditions at $x = m\Lambda + d_1$ and $x = (m+1)\Lambda$:

$$\begin{aligned} E(d_{1-}) &= E(d_{1+}), & \partial_x E(d_{1-}) &= \partial_x E(d_{1+}), \\ E(\Lambda_-) &= E(\Lambda_+), & \partial_x E(\Lambda_-) &= \partial_x E(\Lambda_+), \end{aligned} \quad (2)$$

we obtain

$$\begin{bmatrix} A_{m+1} \\ B_{m+1} \end{bmatrix} = \mathbf{T} \begin{bmatrix} A_m \\ B_m \end{bmatrix}, \quad (3)$$

where \mathbf{T} is the transfer matrix:

$$T_{11} = e^{i\phi_1} (\cos \phi_2 + i\alpha \sin \phi_2), \quad (4a)$$

$$T_{12} = -ie^{-i\phi_1} \beta \sin \phi_2, \quad (4b)$$

$$T_{21} = ie^{i\phi_1} \beta \sin \phi_2, \quad (4c)$$

$$T_{22} = e^{-i\phi_1} (\cos \phi_2 - i\alpha \sin \phi_2), \quad (4d)$$

with $\phi_j = k_j d_j$ ($j = 1, 2$), $\alpha = k_1/k_2 + k_2/k_1$, and $\beta = k_1/k_2 - k_2/k_1$. Together with the well-known Bloch

theorem, $E(x + \Lambda) = e^{ik\Lambda} E(x)$, we have

$$e^{ik\Lambda} \begin{bmatrix} A_m \\ B_m \end{bmatrix} = \mathbf{T} \begin{bmatrix} A_m \\ B_m \end{bmatrix}. \quad (5)$$

To ensure the wave solution exists, we need $\det(\mathbf{T} - e^{ik\Lambda} \mathbf{I}) = 0$ (\mathbf{I} is the identity matrix), from which we have the dispersion relation of the plasma grating:

$$\begin{aligned} \cos k\Lambda &= \left[\cos(k_1 d_1) \cos(k_2 d_2) \right. \\ &\quad \left. - \frac{1}{2} \left(\frac{k_1}{k_2} + \frac{k_2}{k_1} \right) \sin(k_1 d_1) \sin(k_2 d_2) \right], \end{aligned} \quad (6)$$

as shown in Fig. 1(b). The dispersion relation exhibits typical features of a photonic crystal, i.e., it is periodic in the k space and there are infinite frequencies corresponding to a specific k . Most importantly, it has band-gap structures. Writing the electron density as Fourier series: $n = n_0 \left[1 + \sum_{j=-\infty}^{\infty} \eta_j \exp(2\pi jx/\Lambda) \right]$, the theoretical expression of the bandwidth of the lowest band gap can be conveniently obtained [42,43]:

$$\delta\omega \approx \frac{|\eta_1| \omega_c}{1 + n_{cl}/n_0}. \quad (7)$$

One finds the bandwidth is associated with the average density and the coefficient of the first density harmonic, which represents the modulation amplitude of the plasma grating. For the example considered in this section and reproduced in Fig. 1(b) the lowest band gap is from $\omega = 0.888\omega_c$ to $\omega = 1.086\omega_c$ and centered at ω_c , with $\omega_c \sim 1.14\omega_l$. This result is well reproduced by Eq. (7) where $\eta_1 \approx 0.703$ and $\delta\omega \approx 0.162\omega_c$. Lasers with frequency inside the band gap have zero group velocity, which means they will be reflected by the grating when injected into the plasma grating. Lasers with frequency in the band but close to the band-gap edges have very large group-velocity dispersions. So when the plasma grating is suddenly created around the laser (k_l, ω_l), according to the eigenmode transform theory, the laser should conserve its wavevector as k_l , while converting its frequency to the edges of the infinite band gaps at $k = k_l$, light will then be trapped in the grating. The laser frequency will be split to $\omega_{\pm} = \omega_l + \delta\omega_{\pm}$, with $\delta\omega_{\pm} = \omega_l \left[\sqrt{1 + n_0/n_{cl}} (1 \pm |\eta_1| n_0/n_{cl}) - 1 \right]$ or $\omega_l (1/2 \pm |\eta_1|) n_0/n_{cl}$, in the limit $n_0/n_{cl} \ll 1$.

A. Frequency conversion of a free-traveling laser

The interaction between a free-traveling laser and the above-mentioned plasma grating is studied with 1D PIC simulation using the code SMILEI [44]. As shown in Fig. 2(a), the laser has a sinusoidal envelope $a = a_0 \sin(\pi t/T_0)$ with $a_0 = 8.55 \times 10^{-3}$, where a is the laser normalized vector and $T_0 = 20\pi\omega_l^{-1}$. Its wavelength is

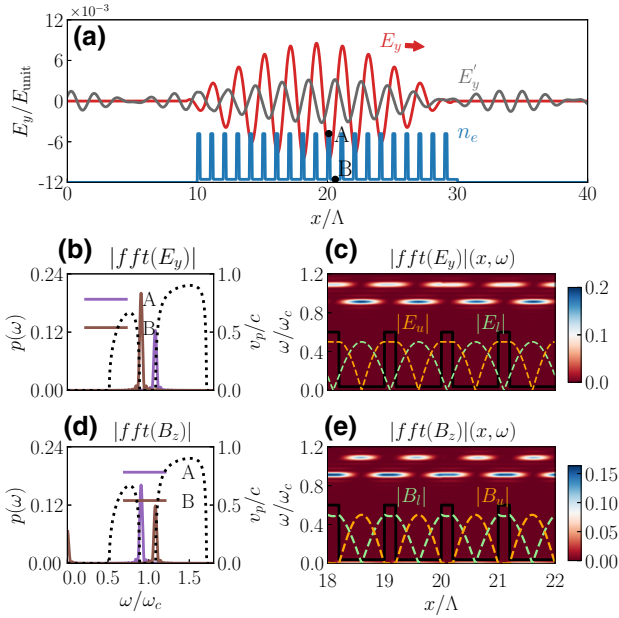


FIG. 2. PIC simulation of frequency conversion of a laser propagating in a suddenly created nonlinear plasma grating. (a) The scheme of a laser interacting with a suddenly created plasma grating. The red line shows E_y at $t = 0$, while the gray line shows E'_y at $t = 100\pi\omega_l^{-1}$. (b) The spectra of E_y at point A and point B labeled in (a) compared with the group velocity of the laser in the plasma grating [shown as the black dotted lines, obtained from the dispersion relation in Fig. 1(b)]. Note at the edges, the group velocities are 0. Point A (B) is at the center of the HD (LD) layer. (c) The spectrum of E_y along x in the center of the simulation box after the plasma grating is initialized. The corresponding plasma density distribution is shown in the low part of the figure, together with the Bloch modes solved from theory. $E_u(E_l)$ is the Bloch mode at the up (low) edge of the lowest band gap. Noting the Bloch modes have been normalized to their maximum amplitude. (d) The spectra of B_z at point A and point B compared with the group velocity of a laser in the plasma grating. (e) The two-dimensional (2D) spectrum of B_z , similar to (c).

$\lambda_l = 2\Lambda$ (and wavevector $k_l = 2\pi/\lambda_l$) and it is linearly polarized along the y axis. The laser is injected into the simulation box from the left boundary. The simulation box has a length of 40Λ . At the beginning of the simulation, there is no plasma grating. When the center of the laser reaches the center of the simulation box at $t = 0$, the plasma grating is initialized. This is approximated by freezing all the particles at the beginning, while unfreezing them from $t = 0$ in PIC simulation. There are 20 grating layers from $x = 10\Lambda$ to $x = 30\Lambda$, which implies a plasma length of $L_p = 20\Lambda$. The cell size is $\lambda_l/128$, 50 particles per species per cell are used with a mass ratio of $m_i/m_e = 1836$ and $Z = 1$. The particles are taken as cold, i.e., $T_e = T_i = 0$ eV.

Shown in Figs. 2(b) and 2(d) are the FFT of E_y and B_z at points A and B [as shown in Fig. 2(a)] for $t > 0$. One finds that the laser frequency has been converted to the

edges of the lowest band gap. Moreover, at point A, E_y is mainly converted to the up edge, whereas at point B it is mainly converted to the low edge, while it is exactly opposite for B_z . One can also find zero-frequency magnetic field at both A and B, which corresponds to the static magnetic field. Up-conversion to higher frequency at the edges of higher-order band gaps is minimal and can be neglected.

The spatial distributions of the spectra of E_y and B_z along x are shown in Figs. 2(c) and 2(e). The electric mode at the up edge of the band gap has more energy in the HD layer, while for the electric mode at the low edge, more energy is localized in the LD layer, and opposite for the magnetic mode. This peculiar energy distribution is one of the characteristics of the eigen Bloch modes at the band-gap edges [42]. Theoretically the Bloch mode E_y can be obtained by finding the eigenvector of Eq. (5) and further determining C_m and D_m through the boundary conditions, i.e., Eq. (2). The magnetic Bloch modes are then obtained with $B_z = (ic/\omega)(\partial E_y/\partial x)$. The distribution of the Bloch modes at the up edge and the low edge of the band gap are shown with $|E_u|$, $|E_l|$ in the superimposed schematic illustration in Fig. 2(b), respectively. The distribution of magnetic Bloch waves are shown in Fig. 2(d) with $|B_u|$, $|B_l|$. The energy distributions of the Bloch modes agree very well with the PIC-simulation results. The Bloch modes have zero group velocity and form standing waves inside the plasma grating, which means the laser is not supposed to exit the plasma grating after the frequency conversion. However, the considered plasma grating is not an ideal periodic medium, it only has a finite number of layers, so the laser energy is slowly “leaking” out from the plasma grating. Still, we can see that after a long time, $t \gg L_p/c$, there is still a considerable portion of the electric energy maintained in the plasma grating, as shown by E'_y in Fig. 2(a) at $t = 100\pi\omega_l^{-1}$, where the laser energy leaving the grating is also visible. Also notice that a “spiky” grating (LD layer is wider than HD layer) is used here, so more laser energy is downshifted than it is upshifted, as one can find in Figs. 2(c) and 2(e). When a regular grating (the width of LD layer is comparable to that of HD layer), e.g., $n_1 = 0.5n_{cl}$, $d_1 = 0.4\Lambda$, $n_2 = 0.167n_{cl}$, $d_2 = 0.6\Lambda$, then the laser energy downshifted is comparable with that upshifted, which is confirmed by PIC simulation (not shown).

Other simulations, in which the laser has different initial frequency and correspondingly wavevector, e.g., (I) $k = 0.5k_l$, (II) $k = 0.9k_l$, (III) $k = 1.1k_l$, (IV) $k = 2k_l$, are also conducted, as shown in Fig. 3. The lasers are found to be mainly converted to the closest eigenfrequency in the dispersion relation of the plasma grating, i.e., (I) mainly to $0.66\omega_c$, (II) mainly to $0.87\omega_c$ and partially to $1.11\omega_c$, (III) mainly to $1.11\omega_c$ and partially to $0.87\omega_c$, (IV) mainly to $1.71\omega_c$ and $1.81\omega_c$, partially to $0.51\omega_c$. When the converted lasers have no zero group-velocity solution, they

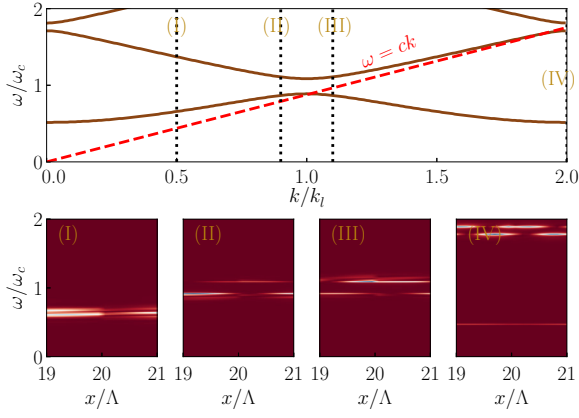


FIG. 3. Frequency conversion of lasers with different initial wavevector: (I) $k = 0.5k_l$, (II) $k = 0.9k_l$, (III) $k = 1.1k_l$, (IV) $k = 2k_l$, with the same simulation setup as shown in Fig. 2. The upper row shows the dispersion relation of the laser in the plasma grating (solid line) compared with that in vacuum (red broken line). The lower row shows the laser-frequency distribution at $x \in (19\Lambda, 21\Lambda)$ after the plasma grating is loaded.

soon get out of the plasma grating (cases I, II, III) and have no energy localization (not shown).

In a realistic situations, the plasma grating cannot be created instantaneously, but it always has a finite growth time. The growing process can be seen as infinitesimal small steps of sudden transitions to plasma gratings with larger and larger modulation amplitude. From here on we focus only on the case where the laser wavelength is λ_l , and the laser energy is localized in the plasma grating after frequency conversion. This energy localization helps the frequency conversion as the plasma grating grows. Instead in the other cases in which the laser group velocity is not 0, the laser quickly leaves the plasma grating and frequency conversion does not happen anymore. Notice also that in the case of λ_l , the frequency-conversion amplitude can be conveniently calculated by Eq. (7).

B. Frequency conversion of beating counterpropagating lasers

Next we consider the action of a “sudden” grating in the presence of two beating counterpropagating lasers. This situation is similar to the case where the laser is created in the framework of SC SBS and for convenience we define these lasers as “pump” lasers. The results of the PIC simulation of this situation are shown in Fig. 4. In addition to the original right-going laser, another laser with the same properties is injected at the right boundary of the simulation box. They beat with each other at $t = 0$, and subsequently the plasma grating is initialized, as shown in Fig. 4(a). The total electric field can be expressed as $E_t = E_0 \cos(k_l x - \omega_l t) + E_0 \cos(-k_l x - \omega_l t + \Delta\phi) = 2E_0 \cos(k_l x - \Delta\phi/2) \cos(\omega_l t - \Delta\phi/2)$. In analogy to the laser-driven plasma grating via SC SBS,

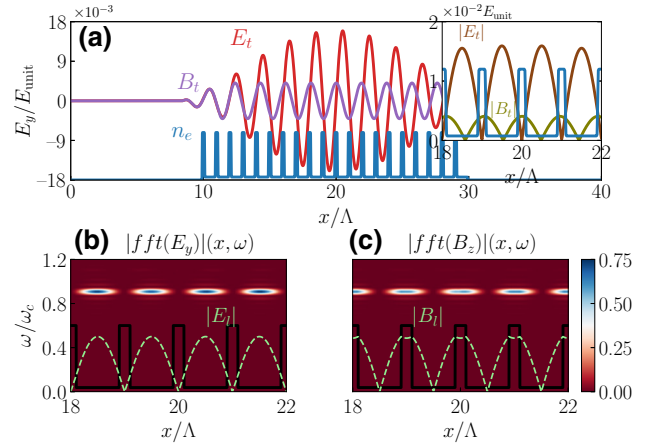


FIG. 4. Frequency conversion in the case of two beating lasers, similar to Fig. 2. (a) The scheme of two beating lasers interacting with a suddenly created plasma grating. E_t and B_t are the total electric field and magnetic field at $t = 0$. The inset shows energy distribution of electric field and magnetic field in the center of the plasma grating. (b),(c) The frequency distribution of the electric field and magnetic field after the plasma grating is initialized at $t = 0$, respectively.

where the particles accumulate in the trough of the ponderomotive potential and form the HD layer, the plasma grating here is intentionally positioned in space to place the HD layers in the center of the trough of the interference pattern, as shown by the inset in Fig. 4(a). This setup corresponds to a phase $\Delta\phi = (2N + 1)\pi$, where N is an integer number. Figure 4(a) also shows the total magnetic field, based on the Faraday function, it can be expressed as $B_t = (2ck_l/\omega_l)E_0 \sin(k_l x - \Delta\phi/2) \sin(\omega_l t - \Delta\phi/2)$, the phase of which in space is $\pi/2$ different from that of the electric field E_t . This explains the fact that after the plasma grating is initialized, only frequency conversion to the low edge of the band gap is found, as shown in Figs. 4(b) and 4(c): in the case of beating lasers, the electric field’s energy is concentrated in the LD layer, while the magnetic field’s energy is concentrated in the HD layer. Their way of energy distribution is exactly the same as the Bloch modes at the low edge of the band gap, i.e., $|E_l|$ and $|B_l|$ after the plasma grating is initialized.

In conclusion, we show by PIC simulation in a suddenly created nonlinear plasma grating with the grating period being half of the laser wavelength, a free-traveling laser converts to long-standing Bloch waves with frequency at up edge and low edge of the lowest band gap. The up Bloch mode’s electric energy is mainly localized in the HD layer while its magnetic energy is mainly localized in the LD layer. The situation is exactly opposite for the low Bloch mode. For both up and low Bloch modes, the space phases of the electrical field and the magnetic field have a difference of $\pi/2$. Instead for two beating counterpropagating lasers, only frequency down-conversion to the low edge of

the lowest band gap happens, their energy distribution is exactly the same as the Bloch modes at the low edge of the band gap.

III. FREQUENCY CONVERSION IN A DYNAMIC PLASMA GRATING DRIVEN BY LASERS VIA SC SBS

A plasma grating can be created in the laboratory by the beating of counterpropagating lasers via SC SBS in an underdense plasma, and can be used as an optical device to manipulate short and intense lasers. The mechanism of the plasma grating's formation and its nonlinear dynamics have been investigated in details in previous studies [29,32]. As opposed to the ideal suddenly created and time-invariant plasma grating, the laser-driven plasma grating first grows up to a maximum value, has a finite lifetime and eventually collapses. The typical dynamic timescale is on the order of hundreds of femtoseconds, depending on the initial parameters (pump frequency, laser amplitude, and plasma density, etc.). In this section, we perform 1D PIC simulations of such dynamic plasma grating and study the frequency conversion of the laser in such a system. We consider two different setups: first the frequency conversion of the pump lasers, and then the frequency conversion of a third free-traveling test pulse. These setups lead to different possible applications of laser-driven plasma grating thanks to their ability to modify the frequency.

A. Frequency conversion of beating pump lasers

We first consider a homogeneous plasma slab of length $L_p = 100k_0^{-1}$ with a density of $n_0 = 0.81n_c$, placed at the center of the simulation box, and surrounded by two $20k_0^{-1}$ vacuum regions. Two identical pump lasers are injected from each side of the simulation box at $t = 0$. Here, ω_0 , k_0 , λ_0 , and n_c are the original frequency of the lasers, wavevector, wavelength in vacuum, and the critical density corresponding to λ_0 : $n_c = m_e \pi c^2 / e^2 \lambda_0^2$, respectively. $k_l = k_0 \sqrt{1 - n_0/n_c}$ and $\lambda_l = \lambda_0 / \sqrt{1 - n_0/n_c}$ are the laser wavevector and laser wavelength in the homogeneous plasma. The pump lasers will beat and drive a fast-evolving plasma grating, the grating size (i.e., the grating width and peak density) evolves rapidly in time, but the grating period $\Lambda = \lambda_l/2$ and average density $\bar{n} = n_0$ are stationary [29,32]. According to the theory in Sec. II the central frequency ω_c is also stationary, because it is only related to Λ and n_0 by $\omega_c = ck_l \sqrt{1 + n_0/n_{cl}}$, and it coincides with the pump-laser frequency $\omega_c = \omega_0$. While the bandwidth of the lowest band gap, which depends on the grating size by Eq. (7), evolves rapidly as the grating evolves.

The linearly polarized pump lasers are constant in time with amplitude $a_0 = 0.2$, except a linearly growing front in $t \in (0, 10\omega_{PE}^{-1})$, where ω_{PE} is the plasma frequency corresponding to n_0 , and duration of $T_p = 400\omega_0^{-1}$. The

initial electron temperature and ion temperature are $T_e = 610$ eV and $T_i = 50$ eV, which makes $\mu = 3T_e/mv_0^2 \approx 0.09$, where μ is a dimensionless parameter determining the grating's dynamics [29,32] and v_0 is the electron oscillation velocity in the pump laser. The spatial resolution is 16 cells per k_0^{-1} and 50 particles per species per cell are used. We label this simulation as case I.

According to our previous studies on the mechanism of plasma-grating formation and dynamics [29,32], the grating dynamic is in the transition regime. By considering the nonlinear model of the plasma-grating formation [29,32] (see Fig. 5 in Ref [32]), the grating should obtain its maximum amplitude of $n_{\max} \approx 5n_0 = 4.05n_c$ at $t = 1.75t_{\text{unit}} + t_0 \approx 723\omega_0^{-1}$ with $t_{\text{unit}} = \sqrt{m_i/2Zm_e}(k_l a_0 c)^{-1} \approx 347.5\omega_0^{-1}$ (obtained from the numerical solution of the model) and $t_0 = L_p/2v_g \approx 115\omega_0^{-1}$ is the time for the laser fronts to reach the plasma center with group velocity $v_g = c^2 k_l / \omega_0$.

The large values of the grating obtained will result in a large band-gap width according to Eq. (7), and eventually big frequency conversion. This is convenient for the theoretical analysis and has motivated the choice of a high value for the initial plasma high plasma density ($n_0 = 0.81n_c$).

The results of the simulation are shown in Fig. 5 where the evolution of the plasma grating is displayed as a function of time, and they agree well with the theoretical estimates. First, the pump lasers beat and form a spatially static and periodic ponderomotive potential. Under the drive of the potential, the electrons drag the ions through electrostatic force and move towards the potential trough, a plasma grating starts to form at about $t = 300\omega_0^{-1}$. At about $t = 750\omega_0^{-1}$, the grating grows to its maximum amplitude of $4.2n_c$. For this density the growth length of SC SBS is $c\gamma_{SC}^{-1} \approx 77k_0^{-1}$, where γ_{SC} is the growth rate of SC SBS [45], of the same order of the plasma length and the energy exchange between the pump lasers is small. As the particles accumulate, the thermal potential also grows rapidly, which then reflects the particles and causes the

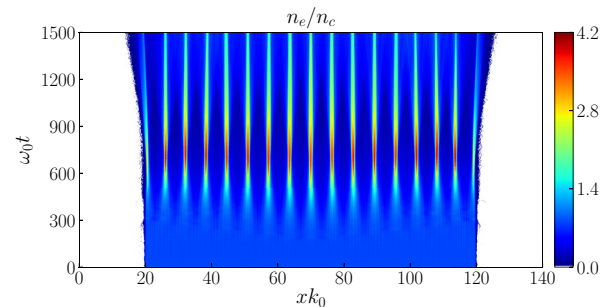


FIG. 5. Case I: density evolution of the plasma grating in time, under the drive of two counterpropagating lasers. Note that $n_e/n_c < 0.02$ is set to be white.

grating to expand, and the grating amplitude to decrease. These are exactly the typical characteristics of the early stage of the transition regime [29,32]. Note here we focus only on the early stage where the plasma grating forms and grows, i.e., $t \leq 650\omega_0^{-1}$; details of the plasma-grating dynamics at later times are discussed in Refs. [29,32].

Once the grating forms, its dispersion relation develops a band-gap structure. The lowest band gap is around ω_0 [20,26], which is similar to the one shown in Fig. 1(b). As the grating grows, the grating's dispersion relation changes and the band-gap width also grows. The frequency of the original pump lasers is in the forbidden zone of the grating. Indeed, considering longer pump-laser duration, $T_p = 1500\omega_0^{-1}$, it is found that the pump lasers after $400\omega_0^{-1}$ are completely reflected, while the grating dynamics are almost unaffected. The generation of plasma grating can be seen as a sudden transition from a homogeneous plasma to a small plasma grating, then infinitesimal small steps of sudden transitions to plasma gratings with larger modulation amplitude. Based on Sec. II, one can expect that the pump lasers will convert their frequencies to the low edge of the lowest band gap. More importantly, the pump lasers can be stored inside the grating due to the zero group velocity at the edges and constantly convert their frequencies to the low edge of the band gap with growing width.

The frequency evolution of electrical field of the pump laser E_y is analyzed, as shown in Fig. 6. The conversion of the laser frequency is clearly seen and the frequency

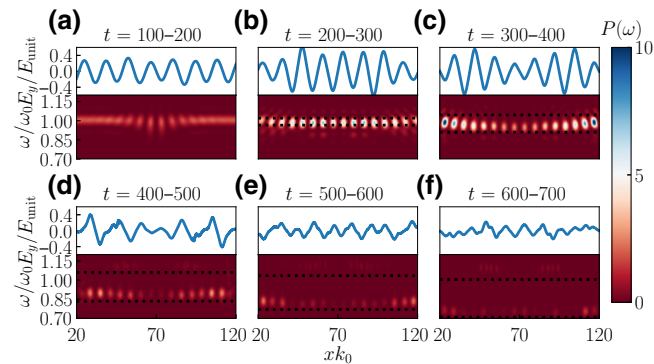


FIG. 6. Evolution of the pump lasers in the growing plasma grating. In each subfigure, the lower panel shows the frequency distribution of E_y , denoted by the power spectral density per ω_0^{-1} (obtained from the FFT) as a function of the x axis in the plasma. The FFT time intervals (in unit of ω_0^{-1}) are labeled in the titles. While the upper panel (blue line) shows the transverse-field distribution and show the interference patterns of the driving lasers in space at the central time in the FFT interval, e.g., $t = 150\omega_0^{-1}$ for figure (a). The black dotted lines show the edges of the lowest band gap for $k/k_l = 1$, obtained by solving numerically via the Fourier approach [20,26,42] the dispersion relation with the periodic density grating obtained in the PIC simulations at the corresponding time (reproduced in Fig. 5).

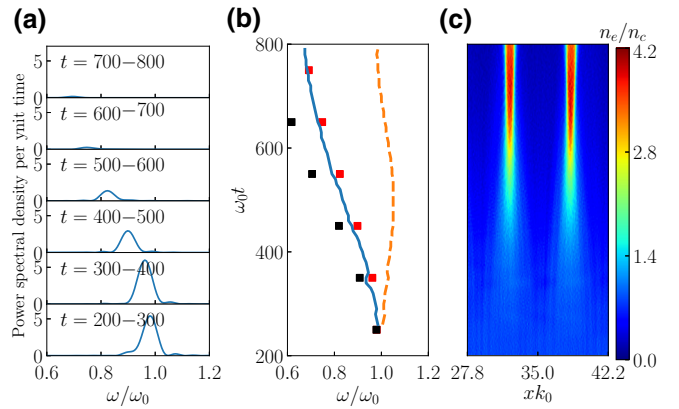


FIG. 7. (a) The laser-frequency evolution at $x = 35k_0^{-1}$. (b) The laser-frequency evolution at $x = 35k_0^{-1}$ compared with the band-gap evolution, the blue line (orange line) is the low (up) edge of the band gap obtained by solving the dispersion relation using the plasma-density information in (c). The red squares are the peaks of the laser frequency in the left figure at the corresponding times, while the black squares are the low edge of the band gap calculated through Eq. (7). (c) The plasma-density evolution around $x = 35k_0^{-1}$ in time.

of the downshifted components agrees well with the low edge of the band gap (shown with the low black dotted line), while no significant up-conversion is found. This frequency conversion is more clearly seen by analyzing the electrical field of the pump laser E_y at $x = 35k_0^{-1}$, as shown in Fig. 7. Figure 7(a) shows the local pump laser constantly downshifts its frequency and its energy is slowly “leaking out” of the grating, because the plasma grating only has a finite number of layers. So in principle, by using a longer plasma with more grating layers, more laser energy can be frequency downshifted. This is confirmed by another simulation (labeled as case A) with a plasma length $L_p = 150k_0^{-1}$, while other parameters are the same as case I (not shown). Figure 7(b) shows the band-gap evolution: the dispersion relation corresponding to the solid blue and dashed orange line in the figure is solved based on the plasma density in Fig. 7(c) by considering the numerical solution via the Fourier approach [20,26,42]. This is the same technique used to obtain the black dotted lines in Fig. 6. As the grating grows and the band gap widens, the frequency conversion obtained in the simulations (red squares) closely follows the low edge of the band gap. The trend is very well reproduced by the formula obtained in Eq. (7) (black squares), calculated here for $\eta_1 = (1/\Lambda) \int_{x_1}^{x_2} n_e(x) e^{i2\pi x/\Lambda} dx$ and $n_{c1} = n_c - n_0$, where $x_1 = 35k_0^{-1}$ and $x_2 = x_1 + \Lambda$, even if the value of the downshift is overestimated, which is attributed to the affects of the higher harmonics.

Next, we perform a PIC simulation with smaller initial plasma density $n_0 = 0.3n_c$ labeled as case II. In this case as well we can estimate the characteristics of the grating

and apply Eq. (7). The frequency conversion of the laser in the dynamic plasma grating can be predicted based on the laser and plasma parameters, and although the downshift is smaller than in the previous case, it follows the same pattern. The PIC-simulation parameters are the same as those of case I, except for the plasma density ($n_0 = 0.3n_c$). We also increase the plasma length to $L_p = 300k_0^{-1}$. Since the growth length of SC SBS for this case is $c\gamma_{SC}^{-1} \approx 69k_0^{-1}$ [45], now the plasma length L_p is larger than the growth length of SC SBS. As a consequence there is some energy exchange between the pulse slowing down the grating formation, however because of the increased length the pump-laser energy can be stored inside the plasma grating for a longer time.

The density evolution of the plasma grating in time is shown in Fig. 8. Large-amplitude density grating starts to form at about $t = 300\omega_0^{-1}$ and grows to its maximum amplitude of $n_{\max} = 1.5n_c$ at about $t = 600\omega_0^{-1}$. Again, according to the nonlinear model of the plasma-grating formation in our previous work [29,32], the grating should obtain its maximum amplitude of $n_{\max} \approx 5n_0 = 1.5n_c$ at $t = 1.75t_{\text{unit}} + t_0 \approx 496\omega_0^{-1}$ with $t_{\text{unit}} = \sqrt{m_i/2Zm_e}(k_1 a_0 c)^{-1} \approx 181\omega_0^{-1}$ and $t_0 \approx 179\omega_0^{-1}$ is the time for the laser fronts to reach the plasma center with group velocity v_g . The model agrees well with the PIC simulation but it underestimates the time to obtain the maximum amplitude. As mentioned above, this is attributed to the energy exchange between the counterpropagating lasers in the large plasma length considered for this case, which is not included in the theoretical model. A significant part of the laser energy is frequency converted to the low edge of the band gap, as shown in Fig. 9. The amplitude of the frequency conversion is much smaller than that of case I, which is expected due to much lower plasma density $n_0 = 0.3n_c$ and smaller band-gap width according to Eq. (7).

The electrical field E_y at $x = 150k_0^{-1}$ is analyzed in detail as a function of time in Fig. 10. The frequency conversion is clearly seen in Fig. 10(a) and is reduced to about $0.917\omega_0$ in the time interval $t = (600 - 700)\omega_0^{-1}$. But the laser energy decreases for the most downshifted values as

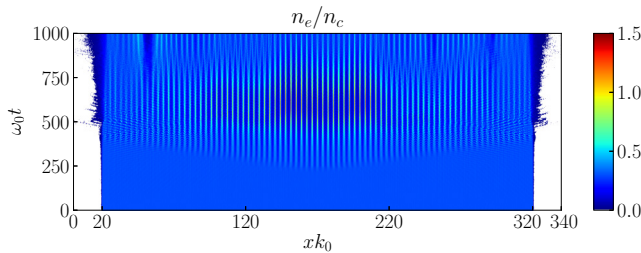


FIG. 8. Case II: density evolution of the plasma grating in time, under the drive of two counterpropagating lasers. Note that $n_e/n_c < 0.01$ is set to be white.

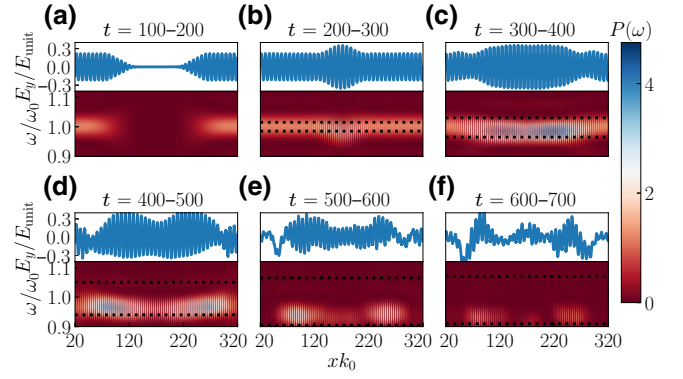


FIG. 9. Case II: evolution of the driving lasers in a growing plasma grating. As in Fig. 6 in each subfigure, the lower panel shows the frequency spectrum of E_y , while the upper panel (blue line) shows snapshots of the driving lasers at the central time of the FFT intervals. The black dotted lines show the edges of the lowest band gap derived from the density pattern obtained in the simulations.

the pulse is moving out from the plasma grating. The conversion frequency agrees well with the low edge of the band gap as shown in Fig. 10(b), the band-gap structure is obtained by solving the dispersion relation of the evolving plasma grating shown in Fig. 10(c).

B. Frequency conversion of a free-traveling test pulse

We consider again the setup corresponding to case I, resulting in the generation of the grating reproduced in Fig. 5. However, now a test pulse with frequency $\omega = \omega_0$

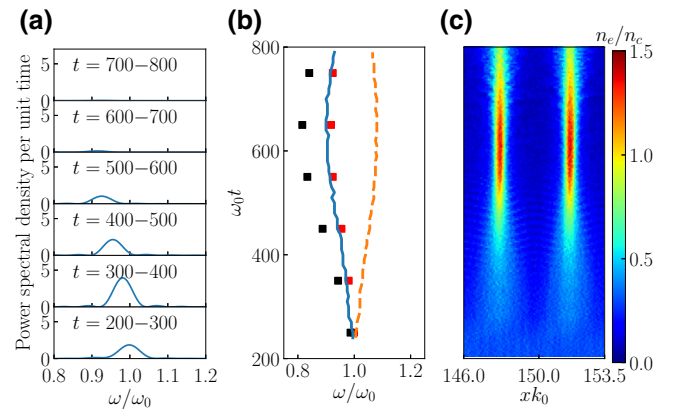


FIG. 10. (a) The laser-frequency evolution at $x = 150k_0^{-1}$. (b) The laser-frequency evolution at $x = 150k_0^{-1}$ compared with the band-gap evolution, the blue line (orange line) is the low (up) edge of the band gap obtained by solving the dispersion relation using the plasma-density information in (c). The red squares are the peaks of the laser frequency in the left figure at the corresponding times, while the black squares are the low edge of the band gap calculated through Eq. (7). (c) The plasma-density evolution around $x = 150k_0^{-1}$ in time.

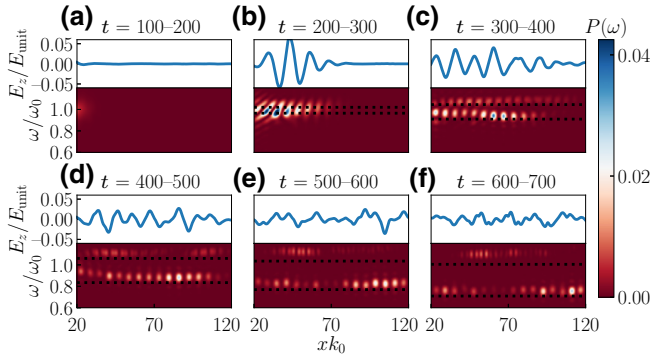


FIG. 11. Evolution of the frequency of the test pulse in the growing plasma grating. As in Fig. 6 in each subfigure, the lower panel shows the frequency spectrum of E_y , while the upper panel (blue line) shows snapshots of the driving lasers at the central time of the FFT intervals. The black dotted lines show the edges of the lowest band gap for the density pattern obtained in the simulations.

is injected into the left boundary of the simulation box at $t_{\text{inj}} = 100\omega_0^{-1}$, as shown in Fig. 11. Its polarization is along the z axis (orthogonal to the polarization of the pump lasers), to ensure that it does not interact with the pump lasers and any frequency conversion can only be induced by the fast-evolving plasma grating. Its amplitude and duration (FWHM, Gaussian) are $a_1 = 0.04$ and $T_{\text{TP}} = 50\omega_0^{-1}$. Note that the injection time and pulse duration need to satisfy the relation: $t_{\text{inj}} + T_{\text{TP}} < t_{\text{start}}$ and $t_{\text{inj}} > t_{\text{start}} - L_p/v_g$ to ensure that the entire test pulse is in the plasma when the grating is generated, where $t_{\text{start}} = 300\omega_0^{-1}$ is the time the grating starts to form. As clearly shown in Fig. 11, the test pulse converts its frequency to both the up and low edges of the band gap, which is constantly widening as the plasma grating grows, and even after $t = 700\omega_0^{-1} \gg L_p/c$, there is still a big portion of the energy of the test pulse stored inside the grating. Moreover, one finds that the electrical mode at the up (low) edges of the band gap store its energy in the HD (LD) layer, just as found in Sec. II, especially clear in Figs. 11(c) and 11(d). The magnetic modes also obey the rule found in Sec. II (not shown here). Notice that the black dotted lines, as in Fig. 6, correspond to the dispersion relation as obtained from the density evolution for case I, shown in Fig. 5. The presence of a test pulse does not affect the grating evolution, so that the value of the expected upshifted and downshifted frequency is unchanged.

This result is consistent with the findings of Sec. II: it is shown there that if the beating (pump) lasers are such that the electric (magnetic) field's energy is concentrated in the LD (HD) layer, this distribution is exactly the same as the Bloch modes at the low edge of the band gap, and only frequency downshift is observed. The test pulse, initially a free-traveling wave at the beginning, does not have

a preferential energy distribution and the electric and magnetic energy access both the HD layers and LD layers. Thus the test pulse has frequency splitting to both the up and low edges of the band gap.

As we can see in Fig. 11 the test pulse is modified so that the intensity of the frequency downshifted part is more significant than the intensity of the upshifted one. This is due to the fact that the dimensionless parameter $\mu = 3T_e/mv_0^2 \simeq 0.09$ is quite small, which implies that the generated grating will be “spiky” [29,32]. In this case, the LD layer is much wider than the HD layer, and more energy is frequency downshifted than it is upshifted. For a larger value of μ instead we expect the grating to be more smooth and the frequency upshift and downshift comparable. We thus consider a smaller laser amplitude $a_0 = 0.0632$, so that $\mu \simeq 0.9$. We denote this as case B. All other parameters are unchanged, except a longer plasma $L_p = 150k_0^{-1}$ is used, which is to compensate the faster “leaking out” of the laser energy, since weaker pump pulses are considered and the dynamic timescale of the grating is longer [32]. According to the theoretical model, the grating should obtain its maximum amplitude of $n_{\text{max}} \simeq 1.78n_0 = 1.44n_c$ at $t = t_0 + 1.63t_{\text{unit}} \simeq 1964\omega_0^{-1}$, while in the simulation the maximum amplitude $n_{\text{max}} \approx 1.69n_c$ is found at $t \approx 1500\omega_0^{-1}$, which agrees quite well with the model. In this situation the widths of the HD layer and LD layer are comparable and as a result, as shown in Fig. 12, the test pulse upshift and downshift are also comparable, and follow closely the dispersion relation obtained from the density evolution.

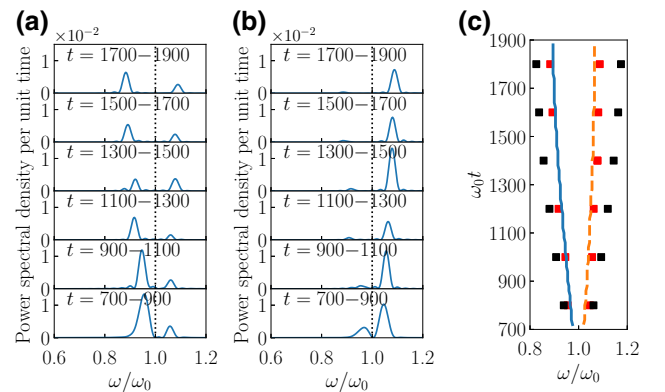


FIG. 12. Frequency evolution of the test pulse in case B (a) at $x = 63.6k_0^{-1}$ (at the center of LD layer), (b) at $x = 67.2k_0^{-1}$ (at the center of HD layer), and (c) the band-gap structure evolution at $x = 63.6k_0^{-1}$. In (c), the left and right red squares are the peaks of the laser frequency in (a),(b) at the corresponding times, respectively. The left and right black squares are the low and high edges of the band gap calculated through Eq. (7).

IV. POSSIBLE APPLICATIONS OF THE OUTGOING LASERS

As the plasma grating forms at around $t_{\text{start}} = 300\omega_0^{-1}$ in case I, both the pump pulses and test pulse are frequency converted and stored inside the plasma grating, part of them leaks out of the grating. The outgoing pump lasers and test pulse are expected to undergo a frequency conversion as well, which is confirmed by analyzing the outgoing laser spectra in the vacuum outside the plasma grating, as shown in Fig. 13(a). The frequency-downshift amplitude of the pump laser is approximately $\delta\omega/2$ with $\delta\omega$ defined by Eq. (7). As the plasma grating grows, this frequency downshift can reach up to 20% (although most of the laser energy is frequency downshifted by just 2%, as shown in Fig. 13). Increasing the plasma length can partially compensate for that and allow more energy in the more downshifted part of the spectrum, as shown by the comparison between case I and case A in Fig. 13(a). We propose that this frequency-downshifted laser can be frequency filtered and used as a seed for backward Raman amplification (BRA) in plasma [46,47]. BRA is a three-wave resonant interaction process and it needs the seed to be slightly but finely detuned from the pump (about 10%) to satisfy the resonance relation: $\omega_p = \omega_s + \omega_{\text{PE}}$, where ω_p , ω_s , and ω_{PE} are the frequencies of the pump laser, seed laser, and the electron plasma wave, respectively. The state-of-the-art optical lasers are restricted at some particular wavelengths for which gain media are readily available, thus the seed in BRA is usually generated by frequency shifting from these wavelengths. This is usually realized by the means of nonlinear optics, using nonlinear media such as gas or crystals [48], the damage threshold of which is very low. Thus the generated seed is so weak that BRA has to go through an inefficient linear stage for a long time until reaching an efficient nonlinear stage, which strongly undermines the amplification efficiency

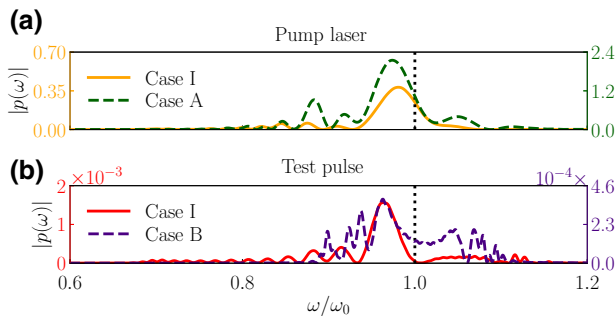


FIG. 13. Spectra of the outgoing pump laser in case I, case A (a) and test pulse (b) in case I, case B after the band gap forms, respectively. They are obtained by performing FFT on the left-going lasers in vacuum. Note that compared to case I, case A uses a longer plasma $L_p = 150k_0^{-1}$ and case B uses smaller pump amplitude $a_0 = 0.0632$ and longer plasma $L_p = 150k_0^{-1}$.

[47,49,50]. The laser-driven plasma-grating method we propose here can not only provide sufficient frequency shift, moreover it uses a medium (i.e., the plasma) with an ultrahigh damage threshold. Intense seed can be generated, which may strongly improve the amplification efficiency [50].

In Fig. 13(b) we show the spectrum of the outgoing test pulse. As we can see a comparable frequency upshift and downshift is obtained in Case B, as discussed in Sec. III. This kind of laser with a frequency split can find useful applications in generating dual-color x rays by Thomson and/or Compton scattering (TCS) of lasers off high-energy electron beams [51–54]. In the head-on colliding geometry and linear TCS regime, the on-axis x-ray frequency is $\omega_x \approx 4\gamma^2\omega_{0\pm}$ [55,56], where γ is the relativistic factor of the electron beam and $\omega_{0\pm}$ is the shifted laser frequency. So using this frequency-split laser for TCS, the generated x ray should have similar frequency split [57] (namely, of two colors). TCS provides high-energy level, relatively compact, and narrow-band x-ray sources. X rays are useful exploring tools in medical, biological, nuclear, and material sciences. Two-color x ray can be further used to monitor and probe the ultrafast changes in atomic, electronic, and magnetic structures simultaneously, or to obtain additional information and discriminates between different compositions [51,58–60]. For example, x-ray imaging is indispensable to detect density-related information of plasma in high energy density physics and inertial confinement fusion, while multicolor x ray can increase the accuracy of electron temperature determination and the detection range of areal densities [61–63]. X-ray crystallography is widely used for structural information of proteins and macromolecules, but it has a bottleneck: phase information [64]. This issue can be addressed by the multi-wavelength anomalous diffraction that employs multicolor x rays as sources [65–67].

For applications of both the outgoing pump laser and test pulse, it is necessary to control their spectral shape, which can be done by controlling the frequency-shift amplitude and the plasma grating's energy-localization ability (characterized by the timescale that the localized laser energy comes out of the plasma grating). The former is associated with the band-gap width, which can be controlled by manipulating the plasma density n_0 and amplitude of the first density harmonic η_1 based on Eq. (7). While η_1 is inversely proportional to $\mu = 3T_{e0}/m_e v_0^2$ [32]. The latter depends on (I) the number of the plasma-grating layers: the more layers, the closer the plasma grating is to an ideal photonic crystal and better energy-localization ability; (II) the timescale of the grating dynamics: the faster the grating evolves, the more laser energy can be frequency shifted before escaping the grating. The grating's dynamic timescale is characterized by $t_{\text{unit}} = \sqrt{(m_i/2Zm_e)}(1/k_l v_0)$ [29,32], which can be controlled by adjusting the pump-laser amplitude and plasma density.

V. CONCLUSIONS

In conclusion, in this paper we study the frequency conversion in a dynamic plasma grating driven by counterpropagating lasers via SC SBS. The laser-driven plasma grating via SC SBS has been studied widely [20,25,26,28,29,32,68–70], because it is a promising optical element to manipulate laser pulses at high intensities (about 5 orders beyond the damage threshold of solid optical elements) and of ultrashort duration (femtosecond to picosecond). It is well known that the dispersion relation of the plasma grating differs significantly from that of a homogeneous plasma. A band gap around the pump frequency is generated after the homogeneous plasma is modulated into such a plasma grating [20,26,68]. Then the original pump lasers are not permitted to exist in the plasma grating, but it was not clear up to now how the pump lasers behave subsequently. This work provides insight on how the pump lasers evolve when the plasma grating is generated and grows.

We find that as the plasma grating grows and the dispersion relation changes in time, the pump lasers convert their frequency to closely follow the low edge of the constantly widening band gap, while their wavelength is kept unchanged so that they still obey the dispersion relation. The lasers can be maintained in the plasma grating for a long time due to their zero group velocity. A similar phenomenon is found with an incident test pulse, but the test pulse converts its frequency to both the up and low edge of the band gap. We attribute the difference to their different energy distribution. We also propose useful applications for laser-driven plasma grating, either to frequency downshift the pump laser to act as a seed for backward Raman amplification, or to frequency split the incident laser to generate dual-color x ray by laser-electron Thomson and/or Compton scattering.

Although the plasma-grating device has useful potential applications, experiments of generation of a controlled and well-characterized plasma grating are still lacking. This is partially due to the fact these kinds of experiments are very demanding on the experimental conditions, as they require multiple, synchronized laser beams and such installations are being commissioned [71,72].

Whereas explaining how the driving lasers interact with the plasma grating will foster its experimental realization. SBS is a widely studied three-wave instability in inertial confinement fusion (ICF), which can consume the energy of the pump laser and is detrimental for the energy coupling. When the speckles of a laser beam focused by a random phase plate in ICF or the intense pump laser in fast-ignition ICF interact with the underdense plasma, the SBS goes into the strongly coupled regime. The late phase of SC SBS is characterized by strongly modulated plasma grating [34,35]. The study that we propose of how the pump lasers evolve in plasma grating implies alternative

features of SC SBS. SC SBS is found to be terminated by the formation of cavitons and cavities in the plasma, which can account for the saturation of SBS at levels of a few percent observed in experiments [34,35]. Our finding about the laser energy localization in the plasma grating and frequency conversion should allow better interpretation of the so-called stimulated-Raman-scattering-like instability, which directly creates the cavitons and cavities [33–35,73,74].

It is also interesting to point out that the scenario of Sec. II, where a laser interacts with a suddenly created plasma grating can have a practical application in the case of a crystal [75–77] or a nanotube [78,79] instantly ionized by x rays. The spatial period of a crystal or a nanotube can be of the same order of the wavelength of an x ray, which then becomes a plasma grating for the x-ray laser after ionization. The interaction of the x-ray laser with crystals or nanotubes is an interesting topic, which might be exploited to realize x-ray wakefield acceleration [75,76,78,80] or x-ray Raman amplification [77].

ACKNOWLEDGMENT

This work is supported by the National Natural Science Foundation of China (NSFC) (Grant No. 12005148) and the Key Laboratory Fund of the Science and Technology on Plasma Physics Laboratory (Grant No. 6142A04200211). This work is conducted within the LABEX Plas@par project, and has received financial state aid managed by the Agence Nationale de la Recherche, as part of the program “Investissements d’avenir” under the reference ANR-11-IDEX-0004-02. S.W. acknowledges support from the project Advanced research using high intensity laser produced photons and particles (ADONIS) (CZ.02.1.01/0.0/0.0/16_019/0000789) and by the project High Field Initiative (HiFI) (CZ.02.1.01/0.0/0.0/15_003/0000449), both from the European Regional Development Fund.

-
- [1] F. R. Morgenthaler, Velocity modulation of electromagnetic waves, *IEEE Trans. Microw. Theory Tech.* **6**, 167 (1958).
 - [2] J. T. Mendonça, *Theory of Photon Acceleration* (CRC Press, 2000).
 - [3] S. C. Wilks, J. M. Dawson, and W. B. Mori, Frequency Up-Conversion of Electromagnetic Radiation with use of an Overdense Plasma, *Phys. Rev. Lett.* **61**, 337 (1988).
 - [4] F. Fiuza, L. O. Silva, and C. Joshi, High-brilliance synchrotron radiation induced by the plasma magnetostatic mode, *Phys. Rev. Spec. Top. Accel. Beams* **13**, 080701 (2010).
 - [5] W. Mori, Generation of tunable radiation using an underdense ionization front, *Phys. Rev. A* **44**, 5118 (1991).
 - [6] W. Mori, Overview of laboratory plasma radiation sources, *Phys. Scr.* **1994**, 28 (1994).

- [7] A. Nerukh and T. Benson, *Non-Stationary Electromagnetics* (CRC Press, 2012).
- [8] D. K. Kalluri, *Electromagnetics of Time Varying Complex Media: Frequency and Polarization Transformer* (CRC Press, 2018).
- [9] E. Yablonovitch, Spectral Broadening in the Light Transmitted Through a Rapidly Growing Plasma, *Phys. Rev. Lett.* **31**, 877 (1973).
- [10] S. Kuo, Frequency Up-Conversion of Microwave Pulse in a Rapidly Growing Plasma, *Phys. Rev. Lett.* **65**, 1000 (1990).
- [11] N. Yugami, T. Niyama, T. Higashiguchi, H. Gao, S. Sasaki, H. Ito, and Y. Nishida, Experimental observation of short-pulse upshifted frequency microwaves from a laser-created overdense plasma, *Phys. Rev. E* **65**, 036505 (2002).
- [12] A. Nishida, N. Yugami, T. Higashiguchi, T. Otsuka, F. Suzuki, M. Nakata, Y. Sentoku, and R. Kodama, Experimental observation of frequency up-conversion by flash ionization, *Appl. Phys. Lett.* **101**, 161118 (2012).
- [13] I. Geltner, Y. Avitzour, and S. Suckewer, Picosecond pulse frequency upshifting by rapid free-carrier creation in ZnSe, *Appl. Phys. Lett.* **81**, 226 (2002).
- [14] Y. Avitzour, I. Geltner, and S. Suckewer, Laser pulse frequency shifting by ionization and recombination fronts in semiconductor plasma, *J. Phys. B: At., Mol. Opt. Phys.* **38**, 779 (2005).
- [15] K. Qu, Q. Jia, M. R. Edwards, and N. J. Fisch, Theory of electromagnetic wave frequency upconversion in dynamic media, *Phys. Rev. E* **98**, 023202 (2018).
- [16] K. Qu and N. J. Fisch, Laser frequency upconversion in plasmas with finite ionization rates, *Phys. Plasmas* **26**, 083105 (2019).
- [17] M. R. Edwards, K. Qu, Q. Jia, J. M. Mikhailova, and N. J. Fisch, Cascaded chirped photon acceleration for efficient frequency conversion, *Phys. Plasmas* **25**, 053102 (2018).
- [18] D. H. Froula, D. Turnbull, A. S. Davies, T. J. Kessler, D. Haberberger, J. P. Palastro, S.-W. Bahk, I. A. Begishev, R. Boni, S. Bucht, *et al.*, Spatiotemporal control of laser intensity, *Nat. Photonics* **12**, 262 (2018).
- [19] A. J. Howard, D. Turnbull, A. S. Davies, P. Franke, D. H. Froula, and J. P. Palastro, Photon Acceleration in a Flying Focus, *Phys. Rev. Lett.* **123**, 124801 (2019).
- [20] G. Lehmann and K.-H. Spatschek, Transient Plasma Photonic Crystals for High-Power Lasers, *Phys. Rev. Lett.* **116**, 225002 (2016).
- [21] H. Hojo and A. Mase, Dispersion relation of electromagnetic waves in one-dimensional plasma photonic crystals, *J. Plasma Fusion Res.* **80**, 89 (2004).
- [22] P. Michel, L. Divol, D. Turnbull, and J. D. Moody, Dynamic Control of the Polarization of Intense Laser Beams Via Optical Wave Mixing in Plasmas, *Phys. Rev. Lett.* **113**, 205001 (2014).
- [23] D. Turnbull, P. Michel, T. Chapman, E. Tubman, B. B. Pollock, C. Y. Chen, C. Goyon, J. S. Ross, L. Divol, N. Woolsey, *et al.*, High Power Dynamic Polarization Control Using Plasma Photonics, *Phys. Rev. Lett.* **116**, 205001 (2016).
- [24] D. Turnbull, C. Goyon, G. E. Kemp, B. B. Pollock, D. Mariscal, L. Divol, J. S. Ross, S. Patankar, J. D. Moody, and P. Michel, Refractive Index Seen by a Probe Beam Interacting with a Laser-Plasma System, *Phys. Rev. Lett.* **118**, 015001 (2017).
- [25] G. Lehmann and K. H. Spatschek, Plasma-based polarizer and waveplate at large laser intensity, *Phys. Rev. E* **97**, 063201 (2018).
- [26] G. Lehmann and K. Spatschek, Laser-driven plasma photonic crystals for high-power lasers, *Phys. Plasmas* **24**, 056701 (2017).
- [27] J. Faith, S. P. Kuo, and J. Huang, Frequency downshifting and trapping of an electromagnetic wave by a rapidly created spatially periodic plasma, *Phys. Rev. E* **55**, 1843 (1997).
- [28] Z.-M. Sheng, J. Zhang, and D. Umstadter, Plasma density gratings induced by intersecting laser pulses in underdense plasmas, *Appl. Phys. B* **77**, 673 (2003).
- [29] H. Peng, C. Riconda, M. Grech, J. Q. Su, and S. Weber, Nonlinear dynamics of laser-generated ion-plasma gratings: A unified description, *Phys. Rev. E* **100**, 061201(R) (2019).
- [30] A. Leblanc, A. Denoëud, L. Chopineau, G. Mennerat, Ph. Martin, and F. Quéré, Plasma holograms for ultrahigh-intensity optics, *Nat. Phys.* **13**, 440 (2017).
- [31] S. Monchocé, S. Kahaly, A. Leblanc, L. Videau, P. Combis, F. Réau, D. Garzella, P. D'Oliveira, Ph. Martin, and F. Quéré, Optically Controlled Solid-Density Transient Plasma Gratings, *Phys. Rev. Lett.* **112**, 145008 (2014).
- [32] H. Peng, C. Riconda, M. Grech, C. Zhou, and S. Weber, Dynamical aspects of plasma gratings driven by a static ponderomotive potential, *Plasma Phys. Controlled Fusion* **62**, 115015 (2020).
- [33] S. Weber, M. Lontano, M. Passoni, C. Riconda, and V. Tikhonchuk, Electromagnetic solitons produced by stimulated Brillouin pulsations in plasmas, *Phys. Plasmas* **12**, 112107 (2005).
- [34] S. Weber, C. Riconda, and V. T. Tikhonchuk, Low-Level Saturation of Brillouin Backscattering due to Cavity Formation in High-Intensity Laser-Plasma Interaction, *Phys. Rev. Lett.* **94**, 055005 (2005).
- [35] S. Weber, C. Riconda, and V. Tikhonchuk, Strong kinetic effects in cavity-induced low-level saturation of stimulated Brillouin backscattering for high-intensity laser-plasma interaction, *Phys. Plasmas* **12**, 043101 (2005).
- [36] M. Bellec, P. Panagiotopoulos, D. G. Papazoglou, N. K. Efremidis, A. Couairon, and S. Tzortzakis, Observation and Optical Tailoring of Photonic Lattice Filaments, *Phys. Rev. Lett.* **109**, 113905 (2012).
- [37] L. Shi, W. Li, Y. Wang, X. Lu, L. Ding, and H. Zeng, Generation of High-Density Electrons Based on Plasma Grating Induced Bragg Diffraction in Air, *Phys. Rev. Lett.* **107**, 095004 (2011).
- [38] Y. Wang, Y. Zhang, P. Chen, L. Shi, X. Lu, J. Wu, L. Ding, and H. Zeng, Generation of high-density electrons based on plasma grating induced Bragg diffraction in air, *Appl. Phys. Lett.* **98**, 111103 (2011).
- [39] J. Liu, W. Li, H. Pan, and H. Zeng, Generation of high-density electrons based on plasma grating induced Bragg diffraction in air, *Appl. Phys. Lett.* **99**, 151105 (2011).
- [40] S. Suntsov, D. Abdollahpour, D. G. Papazoglou, and S. Tzortzakis, Femtosecond laser induced plasma diffraction gratings in air as photonic devices for high intensity laser applications, *Appl. Phys. Lett.* **94**, 251104 (2009).

- [41] L. Plaja and L. Roso, Analytical description of a plasma diffraction grating induced by two crossed laser beams, *Phys. Rev. E* **56**, 7142 (1997).
- [42] B. E. Saleh and M. C. Teich, *Fundamentals of Photonics* (John Wiley & Sons, 2019).
- [43] B. J. Eggleton, C. M. de Sterke, and R. Slusher, Nonlinear pulse propagation in Bragg gratings, *J. Opt. Soc. Am. B* **14**, 2980 (1997).
- [44] J. Derouillat, A. Beck, F. Pérez, T. Vinci, M. Chieramello, A. Grassi, M. Flé, G. Bouchard, I. Plotnikov, N. Aunai, *et al.*, Smilei: A collaborative, open-source, multi-purpose particle-in-cell code for plasma simulation, *Comput. Phys. Commun.* **222**, 351 (2018).
- [45] M. Chieramello, C. Riconda, F. Amiranoff, J. Fuchs, M. Grech, L. Lancia, J.-R. Marquès, T. Vinci, and S. Weber, Optimization of interaction conditions for efficient short laser pulse amplification by stimulated Brillouin scattering in the strongly coupled regime, *Phys. Plasmas* **23**, 072103 (2016).
- [46] V. M. Malkin, G. Shvets, and N. J. Fisch, Fast Compression of Laser Beams to Highly Overcritical Powers, *Phys. Rev. Lett.* **82**, 4448 (1999).
- [47] J. Ren, W. Cheng, S. Li, and S. Suckewer, A new method for generating ultraintense and ultrashort laser pulses, *Nat. Phys.* **3**, 732 (2007).
- [48] W. Cheng, PhD thesis, Princeton University, 2007
- [49] S. Li, PhD thesis, Princeton University, 2013.
- [50] R. Trines, E. P. Alves, J. Vieira, F. Fiúza, R. A. Fonseca, L. O. Silva, R. A. Cairns, and R. Bingham, New criteria for efficient Raman and Brillouin amplification of laser beams in plasma, *Sci. Rep.* **10**, 1 (2020).
- [51] V. Petrillo, A. Bacci, C. Curatolo, M. Ferrario, G. Gatti, C. Maroli, J. V. Rau, C. Ronsivalle, L. Serafini, C. Vaccarezza, *et al.*, Dual color X rays from Thomson or Compton sources, *Phys. Rev. Spec. Top. Accel. Beams* **17**, 020706 (2014).
- [52] I. Drebot, V. Petrillo, and L. Serafini, Two-colour X-gamma ray inverse Compton back-scattering source, *Europhys. Lett.* **120**, 14002 (2017).
- [53] J. Wenz, A. Döpp, K. Khrennikov, S. Schindler, M. F. Gilljohann, H. Ding, J. Götzfried, A. Buck, J. Xu, and M. Heigoldt, Dual-energy electron beams from a compact laser-driven accelerator, *Nat. Photonics* **13**, 263 (2019).
- [54] Y. Wu, C. Yu, Z. Qin, W. Wang, R. Qi, Z. Zhang, K. Feng, L. Ke, Y. Chen, C. Wang, *et al.*, Dual-color γ -rays via all-optical Compton scattering from a cascaded laser-driven wakefield accelerator, *Plasma Phys. Controlled Fusion* **61**, 085030 (2019).
- [55] E. Esarey, S. K. Ride, and P. Sprangle, Nonlinear Thomson scattering of intense laser pulses from beams and plasmas, *Phys. Rev. E* **48**, 3003 (1993).
- [56] S. K. Ride, E. Esarey, and M. Baine, Thomson scattering of intense lasers from electron beams at arbitrary interaction angles, *Phys. Rev. E* **52**, 5425 (1995).
- [57] Y. Taira and M. Katoh, Gamma-ray vortices emitted from nonlinear inverse Thomson scattering of a two-wavelength laser beam, *Phys. Rev. A* **98**, 052130 (2018).
- [58] A. A. Lutman, R. Coffee, Y. Ding, Z. Huang, J. Krzywinski, T. Maxwell, M. Messerschmidt, and H. D. Nuhn, Experimental Demonstration of Femtosecond Two-Color X-Ray Free-Electron Lasers, *Phys. Rev. Lett.* **110**, 134801 (2013).
- [59] E. Allaria, F. Bencivenga, R. Borghes, F. Capotondi, D. Castronovo, P. Charalambous, P. Cinquegrana, M. B. Danailov, G. De Ninno, A. Demidovich, *et al.*, Two-colour pump-probe experiments with a twin-pulse-seed extreme ultraviolet free-electron laser, *Nat. Commun.* **4**, 1 (2013).
- [60] V. Petrillo, M. P. Anania, M. Artioli, A. Bacci, M. Bellaveglia, E. Chiadroni, A. Cianchi, F. Ciocci, G. Dattoli, D. DiGiovane, *et al.*, Observation of Time-Domain Modulation of Free-Electron-Laser Pulses by Multi-peaked Electron-Energy Spectrum, *Phys. Rev. Lett.* **111**, 114802 (2013).
- [61] F. J. Marshall, P. W. McKenty, J. A. Delettrez, R. Epstein, J. P. Knauer, V. A. Smalyuk, J. A. Frenje, C. K. Li, R. D. Petrasso, F. H. Seguin, and R. C. Mancini, Plasma-Density Determination from X-ray Radiography of Laser-Driven Spherical Implosions, *Phys. Rev. Lett.* **102**, 185004 (2009).
- [62] D. B. Sinars, K. J. Peterson, S. A. Slutz, M. C. Herrmann, P. Y. Edmund, M. E. Cuneo, I. C. Smith, G. R. Bennett, B. W. Atherton, J. L. Porter, *et al.*, Observation of instability growth in a copper Z-Pinch target using two-color monochromatic X-ray backlighting, *IEEE Trans. Plasma Sci.* **39**, 2408 (2011).
- [63] H. Sawada, T. Daykin, H. S. McLean, H. Chen, P. K. Patel, Y. Ping, and F. Pérez, Two-color monochromatic X-ray imaging with a single short-pulse laser, *Rev. Sci. Instrum.* **88**, 063502 (2017).
- [64] Z. Dauter, Current state and prospects of macromolecular crystallography, *Acta Crystallogr., Sect. D* **62**, 1 (2006).
- [65] J. M. Guss, E. A. Merritt, R. P. Phizackerley, B. Hedman, M. Murata, K. O. Hodgson, and C. H. Freeman, Phase determination by multiple-wavelength X-ray diffraction: Crystal structure of a basic "blue" copper protein from cucumbers, *Science* **241**, 806 (1988).
- [66] W. A. Hendrickson, Determination of macromolecular structures from anomalous diffraction of synchrotron radiation, *Science* **254**, 51 (1991).
- [67] S. K. Son, H. N. Chapman, and R. Santra, Multiwavelength Anomalous Diffraction at High X-Ray Intensity, *Phys. Rev. Lett.* **107**, 218102 (2011).
- [68] H.-C. Wu, Z.-M. Sheng, Q.-J. Zhang, Y. Cang, and J. Zhang, Manipulating ultrashort intense laser pulses by plasma Bragg gratings, *Phys. Plasmas* **12**, 113103 (2005).
- [69] H.-C. Wu, Z.-M. Sheng, and J. Zhang, Chirped pulse compression in nonuniform plasma Bragg gratings, *Appl. Phys. Lett.* **87**, 201502 (2005).
- [70] H. Ma, S. M. Weng, P. Li, X. F. Li, Y. X. Wang, S. H. Yew, M. Chen, P. McKenna, and Z. M. Sheng, Growth, saturation, and collapse of laser-driven plasma density gratings, *Phys. Plasmas* **27**, 073105 (2020).
- [71] N. Jourdain, U. Chaulagain, M. Havlík, D. Kramer, D. Kumar, I. Majerová, V. T. Tikhonchuk, G. Korn, and S. Weber, The L4n laser beamline of the P3-installation: Towards high-repetition rate high-energy density physics at ELI-beamlines, *Matter Radiat. Extremes* **6**, 015401 (2021).
- [72] Eli-beamlines (Accessed: 2021-04-26), <https://www.eli-beams.eu/>.
- [73] Z. Liu, X. He, C. Zheng, and Y. Wang, The transition from plasma gratings to cavitons in laser-plasma interactions, *Phys. Plasmas* **16**, 093108 (2009).

- [74] S.-X. Luan, Q.-J. Zhang, and Z.-M. Sheng, The formation of relativistic electromagnetic solitons in plasma Bragg gratings induced by two counter-propagating laser pulses, *Appl. Phys. B* **93**, 793 (2008).
- [75] T. Tajima and M. Cavenago, Crystal X-Ray Accelerator, *Phys. Rev. Lett.* **59**, 1440 (1987).
- [76] Z. Liang, B. Shen, X. Zhang, and L. Zhang, High-repetition-rate few-attosecond high-quality electron beams generated from crystals driven by intense X-ray laser, *Matter Radiat. Extremes* **5**, 054401 (2020).
- [77] V. M. Malkin and N. J. Fisch, Relic Crystal-Lattice Effects on Raman Compression of Powerful X-Ray Pulses in Plasmas, *Phys. Rev. Lett.* **99**, 205001 (2007).
- [78] X. Zhang, T. Tajima, D. Farinella, Y. Shin, G. Mourou, J. Wheeler, P. Taborek, P. Chen, F. Dollar, and B. F. Shen, Particle-in-cell simulation of X-ray wakefield acceleration and betatron radiation in nanotubes, *Phys. Rev. Accel. Beams* **19**, 101004 (2016).
- [79] A. Perera, A. Bonatto, C. Bontoiu, J. Resta-López, V. Rodin, C. Welsch, G. Xia, and G. Yadav, Towards ultra-high gradient particle acceleration in carbon nanotubes, *J. Phys. Conf. Ser.* **1596**, 012028 (2020).
- [80] S. Hakimi, T. Nguyen, D. Farinella, C. K. Lau, H.-Y. Wang, P. Taborek, F. Dollar, and T. Tajima, Wakefield in solid state plasma with the ionic lattice force, *Phys. Plasmas* **25**, 023112 (2018).